Lead-Free Perovskite Semiconductors Based on Germanium-Tin Solid Solutions: Structural and Optoelectronic Properties

Satyawan Nagane,[1] Dibyajyoti Ghosh,[2,5] Robert L. Z. Hoye,[3] Baodan Zhao,[3] Shahab Ahmad,[4]

Alison B. Walker,[2] M. Saiful Islam,[5] Satishchandra Ogale[1]* and Aditya Sadhanala[3]**

[1]Department of Physics and Centre for Energy Science, Indian Institute of Science Education and Research (IISER), Dr. Homi Bhabha Road, Pune 411 008, India.

[2]Department of Physics, University of Bath, Bath BA2 7AY, United Kingdom.

[3]Cavendish Laboratory, University of Cambridge, JJ Thomson Avenue, CB3 0HE, Cambridge, United Kingdom.

[4]Institute for Manufacturing, Department of Engineering, University of Cambridge, 17 Charles Babbage Road, Cambridge CB3 0FS, United Kingdom.

[5]Department of Chemistry, University of Bath, Bath BA2 7AY, United Kingdom.

AUTHOR INFORMATION

Corresponding Author

*m.s.islam@bath.ac.uk, *satishogale@iiserpune.ac.in, *as2233@cam.ac.uk

ABSTRACT Solar cells and optoelectronics based on lead halide perovskites are generating considerable interest, but face challenges with the use of toxic lead. Here, we fabricate and characterize lead-free perovskites based on germanium and tin solid solutions, $CH_3NH_3Sn_{(1-x)}Ge_xI_3$ ($0 \leq x \leq 1$). We show that these perovskite compounds possess bandgaps from 2.0 to 1.3 eV, which are suitable for a range of optoelectronic applications, from single junction devices and top cells for tandems to light emitting layers. Their thermodynamic stability and electronic properties are calculated for all compositions and agree well with our experimental measurements. Our findings demonstrate an attractive family of lead-free perovskite semiconductors with a favorable bandgap range for efficient single junction solar cells.

KEYWORDS Lead-free hybrid perovskite, Tin-Germanium (Sn-Ge) perovskite, band tuning, amplified spontaneous emission (ASE) and mixed metal/alloy hybrid perovskite.

INTRODUCTION

Organic-inorganic hybrid perovskites have attracted a great deal of attention in the scientific and industrial communities due to their phenomenal performance in solar cells and light emitting diodes (LEDs)[1–3]. Their superior optoelectronic properties and long carrier diffusion lengths have produced a sharp rise in power conversion efficiencies (PCEs) from below 10% to 22.1% in a few years[4–7]. The attributes that make perovskite-based optoelectronics especially attractive are the ambipolar nature of charge transport [8], long carrier diffusion lengths [9], high molar extinction coefficient [10], easy bandgap tunability and simple thin-film processability [11,12]. Nevertheless, perovskite-based technologies are not yet attractive for commercial use due, for example, to the inclusion of lead in the highest performing perovskite, $CH_3NH_3PbI_3$, which is highly toxic and could enter the soil and groundwater [13]. Lead-free alternatives focusing on Sn-based perovskites [14–19] have been considered. Other replacements for lead in the perovskite semiconductor include Bi [20], Cu [21], Ag [22] and Sb [21], amongst several elements discussed by Hoye et. al.[23] The aim with these lead-free perovskites is to achieve similar or better optoelectronic properties and stability, as compared to their lead-based perovskite counterparts.

We have synthesized perovskites with Sn and Ge that absorb strongly in the visible region with absorption coefficients in the range of 2 – 5 x 10^4 cm^{-1}. The $CH_3NH_3SnI_3$ perovskite has a bandgap lower than ~1.3 eV, much smaller than the 2.0 eV bandgap of the $CH_3NH_3GeI_3$ perovskite [24,25]. Solar cells with thin-films of these perovskites as active layers produce power conversion efficiencies (PCEs) of ~ 6% and ~ 0.1% respectively [26,27]. This poor performance compared to the Pb based perovskite cells has been attributed to poor atmospheric stability and film coverage [28]. In order to improve the stability, a new strategy was evolved to introduce lead into tin-based perovskites to form a Pb-Sn mixed metal perovskite solid solution [29]. These new

Pb-Sn based perovskite solid solutions have delivered excellent solar cell performance and stability, showing the possibilities of multi-metal based perovskite solid solutions [30]. Moreover, these Pb-Sn based solid solutions possess advanced optoelectronic properties and bandgaps smaller than that of the single metal containing perovskites, for example <1.2 eV for $CH_3NH_3Sn_{0.75}Pb_{0.25}I_3$ [30–33] that are suitable for perovskite-perovskite tandems [34].

RESULTS AND DISCUSSION

In this paper, we report the design, synthesis and optoelectronic characterization of Sn-Ge solid solution hybrid perovskites where we have replaced Pb with Ge in the Pb-Sn solid solutions, and fabricated Sn-Ge based perovskites by simple solution processing and vapor deposition methods. We have varied the metal ion composition (Sn to Ge ratio) in the perovskite matrix and investigated the effect on structural geometry and optoelectronic properties.

First of all, for the synthesis of Sn-Ge mixed alloy hybrid perovskites, we applied the well-known single-step solution processing method. In brief, we prepared a 0.5 mmol stock solution of $CH_3NH_3SnI_3$ (using equimolar ratios of CH_3NH_3I and SnI_2) and $CH_3NH_3GeI_3$ (using equimolar ratios of CH_3NH_3I and GeI_2) in *N*, *N*-dimethylformamide (DMF) and mixed these solutions according the required ratios of metal elements *viz.* Sn and Ge in the perovskite matrix. These solutions form the desired perovskite phase on casting into thin-films. Full details of the synthesis methods and diffraction measurements are given in the SI. Recently, Ju *et. al.* predicted the possibility of realizing a series of mixed Sn-Ge perovskites and calculated the band structures of different combinations such as $CsSn_{0.5}Ge_{0.5}I_3$, $CH_3NH_3Sn_{0.5}Ge_{0.5}I_3$, $Cs_{0.5}(CH_3NH_3)_{0.5}Sn_{0.5}Ge_{0.5}I_3$, $Cs_{0.5}(CH(NH_2)_2)_{0.5}Sn_{0.5}Ge_{0.5}I_3$ and $RbSn_{0.5}Ge_{0.5}I_3$. Amongst these

materials, $RbSn_{0.5}Ge_{0.5}I_3$ was shown to cover almost the whole solar spectrum as does $CH_3NH_3PbI_3$ [35].

Regarding the characterization of crystal structures, Figure. 1 shows the X-ray diffraction (XRD) patterns for $CH_3NH_3SnI_3$, $CH_3NH_3Sn_{0.75}Ge_{0.25}I_3$, $CH_3NH_3Sn_{0.50}Ge_{0.50}I_3$, $CH_3NH_3Sn_{0.25}Ge_{0.75}I_3$, and $CH_3NH_3GeI_3$ perovskites. The XRD patterns for $CH_3NH_3SnI_3$ and $CH_3NH_3GeI_3$ perovskites are well matched with the reported data and show tetragonal (space group *P*4*mm*, no. 99) and trigonal (space group *R*3m, no. 160) unit cells, respectively. For powder samples with 0 – 50% Ge (from hereon this represents atomic % of Ge or Sn in the thin-films), we observed a monotonic shift in the peak positions with composition, along with a monotonic shift in the lattice parameters fit to the whole diffraction pattern using the Pawley method (Fig. S6, SI)[24,25] . With 75% Ge for the powder sample, we observe a transition to the trigonal phase from the splitting of the tetragonal (111) and (012) peaks to the trigonal (003), (20$\acute{1}$), (113) and (211) peaks. There is also a non-monotonic change in the XRD patterns from $CH_3NH_3SnI_3$ to $CH_3NH_3Sn_{0.75}Ge_{0.25}I_3$ to $CH_3NH_3GeI_3$ perovskites. This non-systematic shift in the peaks of XRD patterns is consistent with the change in crystal structure from tetragonal to trigonal due to incorporation of the comparatively smaller Ge^{2+} (ionic radius = 73pm)[36] into a $CH_3NH_3SnI_3$ perovskite matrix (Sn^{2+} ionic radius = 118pm)[37], which leads to a distortion in the structure. From the XRD pattern we found that the (001), (002), (003) and (004) planes are intact in all the pure as well as mixed cases with a slight shift. The 75% Ge ($CH_3NH_3Sn_{0.25}Ge_{0.75}I_3$) perovskite shows more structural features similar to the pure germanium (100% Ge) based perovskite.

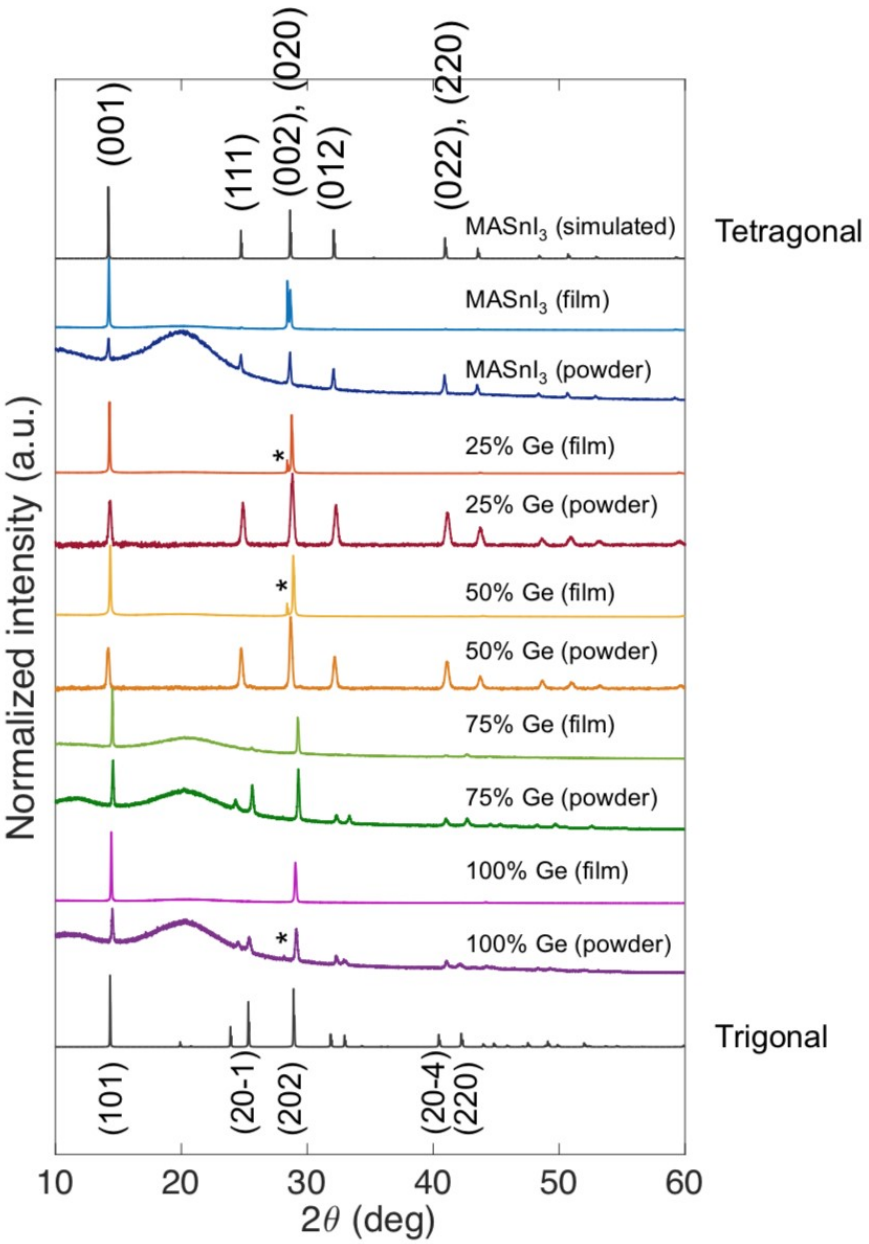

Figure 1. X-ray diffraction (XRD) patterns for 0% Ge ($CH_3NH_3SnI_3$), 25% Ge ($CH_3NH_3Sn_{0.75}Ge_{0.25}I_3$)**,** 50% Ge ($CH_3NH_3Sn_{0.50}Ge_{0.50}I_3$), 75% Ge ($CH_3NH_3Sn_{0.25}Ge_{0.75}I_3$) and 100% Ge ($CH_3NH_3GeI_3$) perovskites for powder and thin-film samples along-with the simulated diffraction pattern. * indicates small impurity phases.

It is known that we can test whether the Goldschmidt tolerance factor (*t*), a semi-empirical geometric parameter, can be linked to the structural stability of the ABX_3 perovskite systems (see SI for details).[38] The tolerance factor values for a range of Ge-Sn compositions are listed in Table 1; they are in the range where the perovskite phase is stable and consequently gives an indication that mixed Sn-Ge perovskites can be created.

A major obstacle for commercialization of hybrid perovskite solar cells is their long-term stability. Therefore, we have examined the energies of decomposition of these materials using *ab initio* simulations. Here, a negative enthalpy value would indicate the greater intrinsic stability of the perovskites over their decomposition products, for example, SnI_2 and CH_3NH_3I for $CH_3NH_3SnI_3$ (calculation details including optimized geometries (Table S2) can be found in SI). The results (also listed in Table 1) show that all the enthalpy values are negative for the $CH_3NH_3Sn_{(1-x)}Ge_xI_3$ system, which indicates favorable energetic stability of these materials in the perovskite phase. These findings directly support the thermodynamic stability of Sn-Ge mixed perovskites, observed experimentally. In order to explore the stability of $CH_3NH_3Sn_{(1-x)}Ge_xI_3$ at finite temperature (300K), we also performed *ab initio* molecular dynamics (AIMD) simulations extending our previous work.[39,40] We find no sign of decomposition of their perovskite structures (simulation snapshots of $CH_3NH_3Sn_{0.5}Ge_{0.5}I_3$ as a representative system are shown in Figure S8). These results again provide support for the intrinsic stability of mixed Sn-Ge perovskites at room temperature under inert atmosphere.

Table 1. Calculated Goldschmidt tolerance factor (t) and enthalpy of decomposition (ΔH) for $CH_3NH_3Sn_{(1-x)}Ge_xI_3$ perovskites.

Systems	*t*	ΔH (meV/f.u.)
0% Ge ($CH_3NH_3SnI_3$)	0.84	-166
25% Ge ($CH_3NH_3Sn_{0.75}Ge_{0.25}I_3$)	0.87	-55
50% Ge ($CH_3NH_3Sn_{0.5}Ge_{0.5}I_3$)	0.90	-48
75% Ge ($CH_3NH_3Sn_{0.25}Ge_{0.75}I_3$)	0.93	-94
100% Ge ($CH_3NH_3GeI_3$)	0.96	-130

We now consider the optoelectronic characteristics of these lead-free materials. Figure 2 shows the optical properties of $CH_3NH_3Sn_{(1-x)}Ge_xI_3$ $[0 \leq x \leq 1]$ perovskite thin films fabricated on quartz substrates. The normalized absorption spectra (Figure 2a) show a monotonic shift in the absorption edge towards higher energies on addition of Ge. We measure a bandgap of ~1.3 eV for the 0% Ge content sample (x = 1.0) and ~1.9eV for the 0% Sn sample (x = 1). With an increase in content of Ge, the bandgap of the material increased (Figure 2a). A blue shift in the photoluminescence spectra whose value increased with increasing Ge content (Figure 2b) was seen in steady state photoluminescence (PL) measurements on films with a single optically active phase.

The 0% Ge content perovskite, $CH_3NH_3SnI_3$, exhibits a PL peak centered at 945 nm. We further observe a monotonic blue shift in the PL spectra from 945 nm for 0% Ge to 640 nm for the 100% Ge perovskite ($CH_3NH_3GeI_3$), with 75%, 50% and 25% Ge samples demonstrating PL at peak wavelengths of 700 nm, 773 nm and 850 nm respectively. We stress that this is the first report that shows PL from a pure germanium perovskite. Figure 2c shows the trend in PL peak position

and band gap of perovskites with varying Ge content. This comparison reveals the small bandgap bowing as observed previously in $CH_3NH_3Sn_xPb_{1-x}I_3$ [$0 \leq x \leq 1$] binary metal perovskites [30,31,33,44]. However, we do not observe that any of these perovskites exhibit a band gap lower than the pure tin perovskite as observed in the case of $CH_3NH_3Sn_xPb_{1-x}I_3$ [$0 \leq X \leq 1$] binary metal perovskites [30–33,44] This difference may be due to the way in which the orbitals of the Pb and Sn couple as compared to that between Sn and Ge, which we discuss further below. In addition, we observe atmospheric instability in these Ge and Sn based perovskites due to oxidation similar to that observed by other Sn based systems [24,43,45,46]. Further investigation might find possible solutions to this issue as is the case with Sn based systems.[34,47–49]

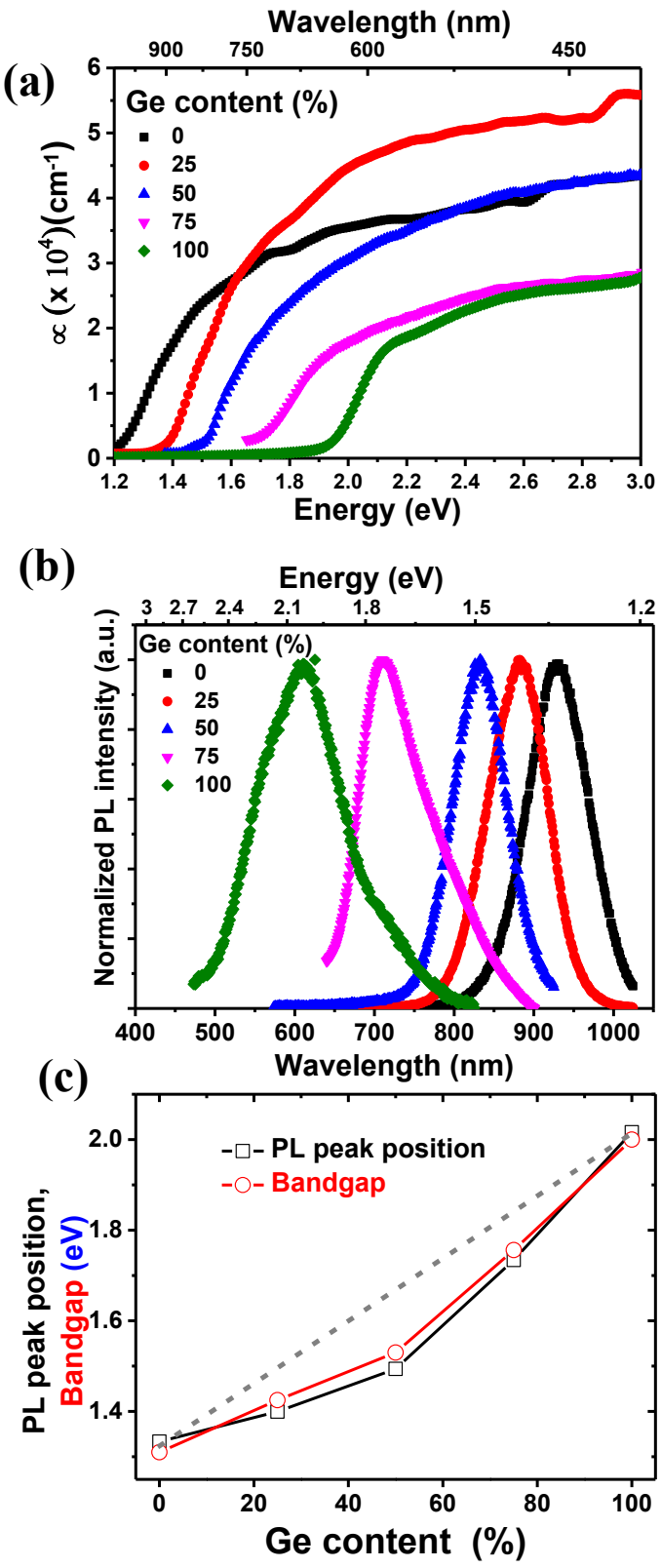
(a)
Wavelength (nm)
900
750
600
450
Ge content (%)
0
25
50
75
100
∝ (x 10^4)(cm^-1)
Energy (eV)
(b)
Energy (eV)
Ge content (%)
Normalized PL intensity (a.u.)
Wavelength (nm)
(c)
PL peak position
Bandgap
PL peak position, Bandgap (eV)
Ge content (%)

Figure 2. Optical properties with change in Ge content (0% to 100%), (a) absorption spectra, note that the non-uniform thin-film morphology causes these values to vary by 10 - 15% due to the thickness values we use for absorption coefficient calculations, (b) normalized photoluminescence (PL) spectra. (c) Comparison of PL peak position and band gap of Sn-Ge perovskites with change in Ge content (0% to 100%).

Figure 3 shows the PL decay measured with varying germanium content in the perovskite. All measurements were done at ~1 Sun illumination intensity and all the data recorded are longer than the instrument response function (IRF) as indicated. The lifetime data was extracted using a bimolecular decay model and are listed in Table 2. We observe that the 0% Ge perovskite demonstrates the fastest initial decay followed by the 25% Ge perovskite. The 50% Ge sample shows a slower initial decay followed by a long decay of ~390 ps. 75% and 100% Ge samples both show slow initial decays of more than half of the charge carriers followed by a delayed recombination of rest. The general trend of faster radiative recombination in lower Ge containing perovskites might be due to the high doping concentration in tin-rich perovskites as observed by others [24,30].

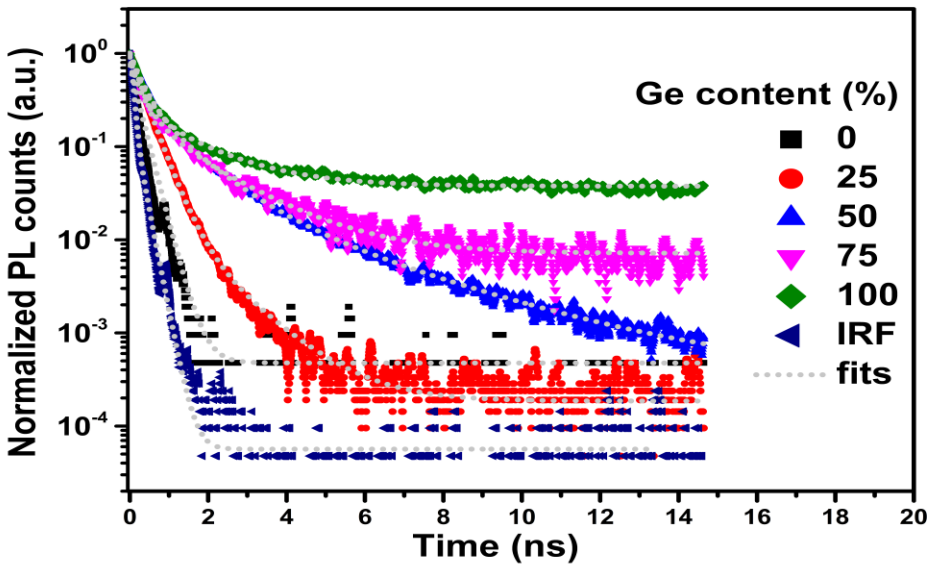

Figure 3. Optical properties - PL decay measured using a 407nm pulsed laser that excited the samples at a fluence of 5 x 10^{14} cm^{-3} with change in Ge content (0% to 100%).

Table 2: Fitted lifetime values using a bimolecular decay model along with the respective % contribution of each component. IRF indicates the instrument response.

Samples	τ_1 (ps)	τ_2 (ps)
0% Ge	140 ± 2 (90%)	620 ± 6 (10%)
25% Ge	570 ± 5 (30%)	320 ± 3 (70%)
50% Ge	1620 ± 15 (54%)	390 ± 4 (46%)
75% Ge	1300 ± 12 (62%)	270 ± 3 (38%)
100% Ge	2100 ± 20 (55%)	360 ± 4 (45%)
IRF	112 ± 2 (100%)	-

To analyze the quality of the perovskite formed, we performed photothermal deflection spectroscopy (PDS) measurements shown in Figure 4a that give the absorption in a semiconductor with a 4-5 orders of magnitude dynamic range sensitivity. This measurement gives us insights into the energetic disorder in the form of an Urbach tail that is a convolution of all sub-band gap defect states arising from intrinsic doping as well as degradation in the materials [30]. From Figure 4a we can see a steep drop in the absorption edges. The PDS spectrum for pure $CH_3NH_3SnI_3$ perovskite shows the smallest bandgap and an Urbach energy of ~54 meV. The bandgap widens with increasing Ge content. The Urbach energy for the 25% Ge sample increases to 54 meV and decreases to 47 meV for the 50% Ge sample (Figure 4b). The Urbach energy further increases to 103 meV for the 75% Ge sample before dropping to 63 meV for $CH_3NH_3GeI_3$. The increase in disorder in the 75% Ge perovskite may be due to the transition in phase from tetragonal to trigonal. Although these Urbach energies are higher than that obtained for $CH_3NH_3PbI_3$ (~14 meV), [41,42] they are in the same range as perovskites that are prone to intrinsic doping and generation of free charge carriers reported earlier [24,25,30,43,44].

We find that the 50% Ge content sample demonstrates the lowest Urbach energy amongst the $CH_3NH_3Sn_{(1-x)}Ge_xI_3$ perovskites and with a decent photoluminescence quantum yield (PLQY) of 2%. Figure 4c also shows the variation in the PL full width at half maxima (FWHM) in comparison with the variation in Urbach energies for all the $CH_3NH_3Sn_{(1-x)}Ge_xI_3$ samples. The two sets of measurements are consistent, indicating the dependence of the PL broadening on the energetic disorder, with 50% Ge perovskite thin-film sample being the stand out semiconductor in the family. This low disorder might be the reason behind the superior optical properties that we observe in the case of 50% Ge content sample, predicted in the recent work by Ju et.al [35].

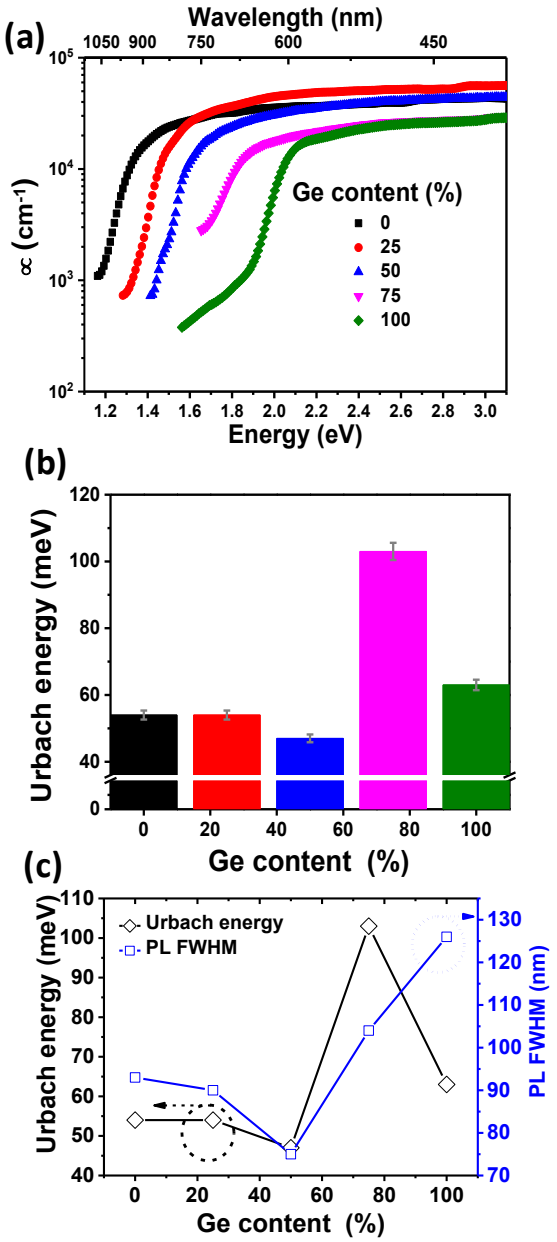

Figure 4. (a) Photothermal deflection spectroscopy (PDS) spectra and the (b) fitted Urbach energy values and (c) comparison of PL FWHM and Urbach energy for the Sn-Ge perovskites with change in Ge content (0% to 100%). Note that there's a 5% error in the Urbach energy values due to the error in fitting the values.

We measured the PL quantum yield (PLQY) for the 50% Ge sample to yield a decent value of 2%. Furthermore, the 50% Ge sample also demonstrates PL narrowing at higher excitation densities, from a full width at half maxima (FWHM) of ~75 nm down to less than half ~40 nm, as shown in figure 5b, a possible demonstration of amplified spontaneous emission (ASE). The 50% Ge sample is a good candidate for various optoelectronic applications owing to its superior optical properties; these include a high absorption coefficient reaching 4 x 10^4 cm^{-1} (Figure 2a), long charge carrier recombination, and a bandgap that covers the entire Vis-NIR spectrum similar to that shown by $CH_3NH_3PbI_3$ and GaAs which is close to optimum for a single junction solar cell.

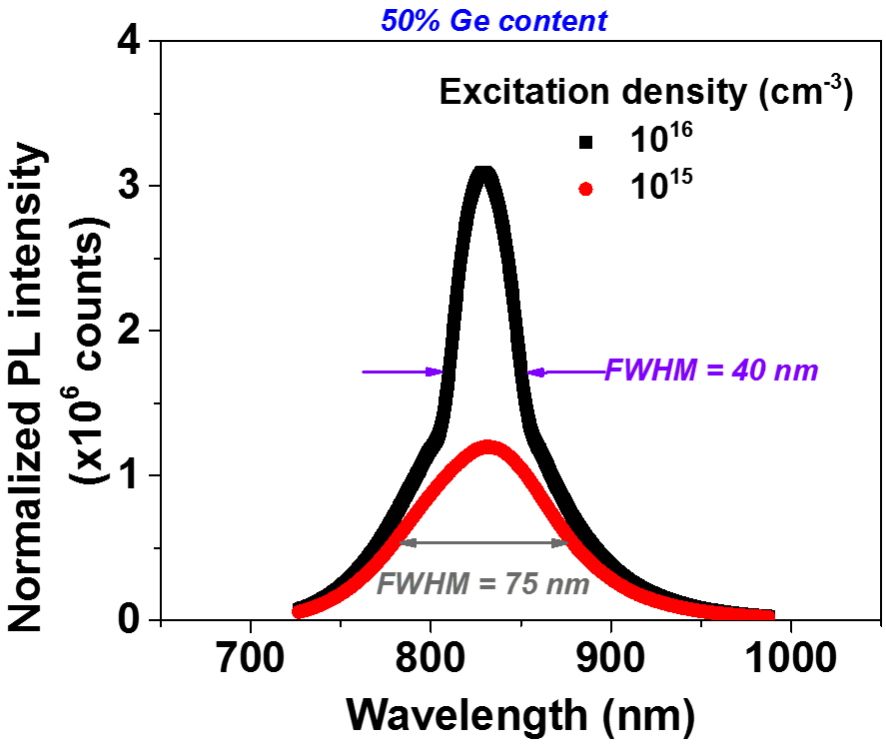

Figure 5. PL of 50% Ge content perovskite thin-film sample with varying excitation densities showing PL narrowing (ASE).

A key property for a material to be used as an efficient absorber for solar cells is the optical band-gap as well as its transition nature. Our a*b initio* DFT calculations show an increase in the band-gap when going from $CH_3NH_3SnI_3$ to $CH_3NH_3GeI_3$ (Table 3 and Figure 6(a)). The variation in band gap with Sn-Ge mixing is consistent with our experimental observations (Figure 5(a)). It should be noted that we also considered inclusion of spin-orbital coupling in our DFT simulations (Table S3 in SI), which significantly underestimates the experimental band gap values, although the trend from $CH_3NH_3SnI_3$ to $CH_3NH_3GeI_3$ remains unchanged. Exploring the band structures of all these perovskites (Figure S9), indicate that they are direct-gap semiconductors.

Table 3. Calculated electronic band-gaps and carrier effective masses for $CH_3NH_3Sn_{(1-x)}Ge_xI_3$ perovskites (using GGA-PBEsol functionals).

Systems	Band Gap (eV)	Effective Mass (m_h^*/m_e)
0% Ge ($CH_3NH_3SnI_3$)	0.50	0.13
25% Ge ($CH_3NH_3Sn_{0.75}Ge_{0.25}I_3$)	0.56	0.12
50% Ge ($CH_3NH_3Sn_{0.5}Ge_{0.5}I_3$)	0.68	0.14
75% Ge ($CH_3NH_3Sn_{0.25}Ge_{O.75}I_3$)	1.20	0.33
100% Ge ($CH_3NH_3GeI_3$)	1.38	0.37

Another important factor which affects the overall performance of these solar cell materials is the transport of photo-generated charge carriers inside the device. We have derived the carrier effective mass (m*), which provides an indication of the carrier mobility (μ) (under a constant relaxation-time approximation through the relation, $\mu=e\tau/m^*$ where e is the elementary charge and τ is the relaxation time. As listed in Table 3, relatively low values are found for the carrier

effective mass for pure and mixed Sn-Ge perovskites (with the lowest values for 0%, 25% and 50%), which suggests good hole transport properties and are important for promising solar cell materials. Despite the lack of experimental data for these compounds for direct comparison, these values are consistent with related hybrid perovskites.[50]

Finally, to examine the nature of the valence and conduction bands of these Sn-Ge mixed perovskites, the density of states (DOS) have been simulated. As can be seen in Figure 6(b-d) (and Figure S10(a,b)), the valence band of the parent perovskite as well as mixed-metal compounds has dominant contributions from 5p orbitals of the I atoms, with additional contributions from the s-orbitals of the B-site metals (i.e. Sn and/or Ge). For the conduction band, the p-orbitals of B-site metal atoms (4p for Ge or 5p for Sn) largely contribute. Interestingly, as we move along the series from $CH_3NH_3SnI_3$ to $CH_3NH_3GeI_3$, the major contributing orbitals to the conduction band changes from Sn 5p-orbitals to Ge 4p-orbitals (shown in Figure 6(b-d) and Figure S10(a,b)). This seems to be the origin of the increase in the band-gap as the Ge content increases in the $CH_3NH_3Sn_{(1-x)}Ge_xI_3$ perovskite solid solution. In addition, for Ge-rich systems, (i.e. x=0.75, 1) the trigonal distortion in the GeI_6 octahedra, leads to half of the Ge-I bond-lengths increasing to ~3.5 Angstrom (Table S2), which reduces the orbital overlap between the B-metal and iodine. Since, the highly dispersive valence band in the halide perovskites appears from the strong metal halide orbital interactions, the elongation of Ge-I bonds leads to less dispersive valence band maxima for these solid-solutions (Figure S9(d)). Such a non-dispersive nature of the valence band also relates to the relatively higher effective mass for the Ge-rich perovskites as shown in Table 3.

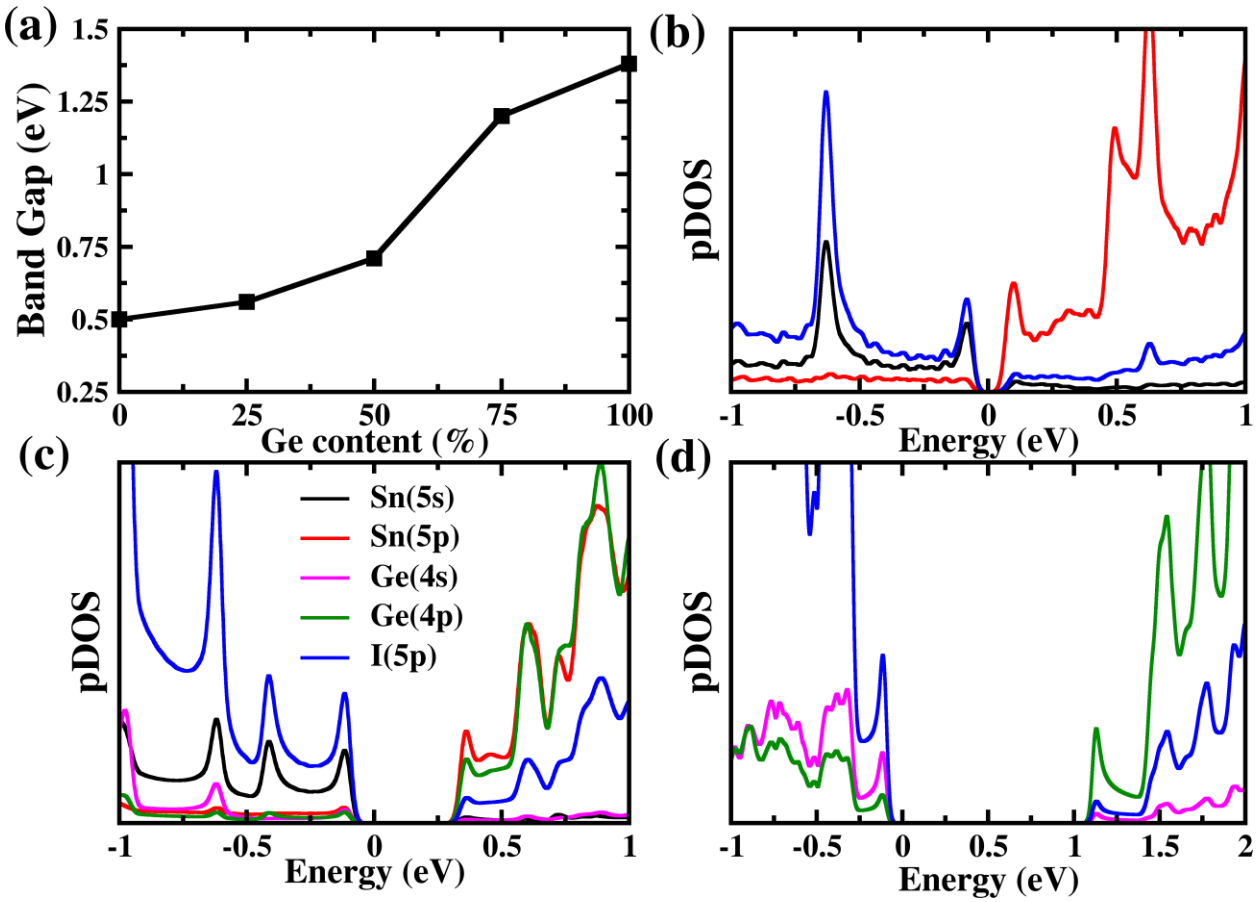

Figure 6. **Electronic properties**. (a) Variation in the calculated bandgaps by tuning the Ge content in $CH_3NH_3Sn_{(1-x)}Ge_xI_3$ perovskites. Projected density of states (pDOS) of (b) 0% Ge ($CH_3NH_3SnI_3$), (c) 50% Ge ($CH_3NH_3Sn_{0.5}Ge_{0.5}I_3$), and (d) 100% Ge ($CH_3NH_3GeI_3$) including SOC.

CONCLUSIONS

In conclusion, we have successfully synthesized and characterized a new germanium-tin based perovskite family, $CH_3NH_3Sn_{(1-x)}Ge_xI_3$ [$0 \leq x \leq 1$]. The addition of germanium to $CH_3NH_3SnI_3$ produces a systematic blue-shift in the band gap from 1.3 eV to 2.0 eV. We also observe simultaneous monotonic shifts in absorption and photoluminescence for the Ge-Sn mixed-metal

perovskites. Ab initio simulations on their intrinsic stability and band gap properties agree well with the experimental observations. The insertion of Ge into $CH_3NH_3SnI_3$ results in an amplified spontaneous emission from the 50% Ge perovskite thin-film. Moreover, the 50% Ge content perovskite also demonstrates the lowest disorder (Urbach energy of ~47 meV) amongst the entire family, while demonstrating a bandgap (~1.5 eV) that is ideal for fabricating an efficient single junction solar cell. We believe that the favorable optoelectronic properties of this family of germanium and tin perovskites will result in the fabrication of novel lead-free perovskite optoelectronics, as well as stimulating further research into alternative lead-free perovskite semiconductors.

ASSOCIATED CONTENT

Supporting Information. Contains molecular dynamics simulation data, energy dispersive X-ray data, SEM, fittings to the optical data and structural data. The Supporting Information is available free of charge on the ACS Publications website.

AUTHOR INFORMATION

Notes

The authors declare no competing financial interests.

ACKNOWLEDGMENT

A.S. would like to thank Prof. Sir Richard Friend and Dr Michael De Volder for the useful discussions. A.S., S.N. and S.O would like to acknowledge the support from Indo-UK APEX project. A.S. would like to acknowledge the support from EPSRC. S.O. would like to acknowledge funding support from DST Nanomission Thematic Unit and DST-CERI programs, Govt. of India. D.G., S.I. and A.B.W. acknowledge the support from Energy oriented Centre of Excellence (EoCoE), grant agreement number 676629, funded within the Horizon2020 framework of the European Union. S.N. and D.G. contributed equally to this work and they worked on performing most of the experiment and theoretical calculations. R. L. Z. H. and B. Z. helped with XRD sample preparation and analysis. S.A. helped in sensitive absorption measurements and SEM data collection. A.B.W. and M.S.I. supervised the theoretical calculations and their interpretation along with D.G. who formulated the calculations. A.S. and S.N. conceptualized the work. S.O. and A.S. further designed and supervised the entire work.

REFERENCES

(1) Shin, S. S.; Yeom, E. J.; Yang, W. S.; Hur, S.; Kim, M. G.; Im, J.; Seo, J.; Noh, J. H.; Seok, S. Il. Colloidally Prepared La-Doped BaSnO3 Electrodes for Efficient, Photostable Perovskite Solar Cells. *Science* **2017**, *356* (6334).

(2) Yuan, M.; Quan, L. N.; Comin, R.; Walters, G.; Sabatini, R.; Voznyy, O.; Hoogland, S.; Zhao, Y.; Beauregard, E. M.; Kanjanaboos, P.; et al. Light-Emitting Diodes. *Nat. Nanotechnol.* **2016**, *11* (10), 872–877.

(3) Li, W.; Wang, Z.; Deschler, F.; Gao, S.; Friend, R. H.; Cheetham, A. K. Chemically Diverse and Multifunctional Hybrid Organic–inorganic Perovskites. *Nat. Rev. Mater.* **2017**, *2* (3), 16099.

(4) Kojima, A.; Teshima, K.; Shirai, Y.; Miyasaka, T. Organometal Halide Perovskites as Visible-Light Sensitizers for Photovoltaic Cells. *J. Am. Chem. Soc.* **2009**, *131* (17), 6050–6051.

(5) Kim, H.-S.; Lee, C.-R.; Im, J.-H.; Lee, K.-B.; Moehl, T.; Marchioro, A.; Moon, S.-J.; Humphry-Baker, R.; Yum, J.-H.; Moser, J. E.; et al. Lead Iodide Perovskite Sensitized All-Solid-State Submicron Thin Film Mesoscopic Solar Cell with Efficiency Exceeding 9%. *Sci. Rep.* **2012**, *2*, 591–598.

(6) Lee, M. M.; Teuscher, J.; Miyasaka, T.; Murakami, T. N.; Snaith, H. J. Efficient Hybrid Solar Cells Based on Meso-Superstructured Organometal Halide Perovskites. *Science*. 2012, pp 643–647.

(7) National Renewable Energy Laboratory. PV Efficiency chart https://www.nrel.gov/pv/assets/images/efficiency-chart.png.

(8) Li, F.; Ma, C.; Wang, H.; Hu, W.; Yu, W.; Sheikh, A. D.; Wu, T. Ambipolar Solution-Processed Hybrid Perovskite Phototransistors. *Nat. Commun.* **2015**, *6*, 8238.

(9) Stranks, S. D.; Eperon, G. E.; Grancini, G.; Menelaou, C.; Alcocer, M. J. P.; Leijtens, T.;

Herz, L. M.; Petrozza, A.; Snaith, H. J. Electron-Hole Diffusion Lengths Exceeding 1 Micrometer in an Organometal Trihalide Perovskite Absorber. *Science* **2013**, *342* (6156), 341–344.

(10) Park, N. Organometal Perovskite Light Absorbers Toward a 20% Efficiency Low-Cost Solid-State Mesoscopic Solar Cell. *J. Phys. Chem. Lett.* **2013**, *4* (15), 2423–2429.

(11) Sadhanala, A.; Deschler, F.; Thomas, T. H.; Dutton, S. E.; Goedel, K. C.; Hanusch, F. C.; Lai, M. L.; Steiner, U.; Bein, T.; Docampo, P.; et al. Preparation of Single-Phase Films of CH 3 NH 3 Pb(I 1– X Br X) 3 with Sharp Optical Band Edges. *J. Phys. Chem. Lett.* **2014**, *5* (15), 2501–2505.

(12) Sadhanala, A.; Ahmad, S.; Zhao, B.; Giesbrecht, N.; Pearce, P. M.; Deschler, F.; Hoye, R. L. Z. Z.; Gödel, K. C.; Bein, T.; Docampo, P.; et al. Blue-Green Color Tunable Solution Processable Organolead Chloride–Bromide Mixed Halide Perovskites for Optoelectronic Applications. *Nano Lett.* **2015**, *15* (9), 6095–6101.

(13) Babayigit, A.; Ethirajan, A.; Muller, M.; Conings, B. Toxicity of Organometal Halide Perovskite Solar Cells. *Nat. Mater.* **2016**, *15* (3), 247–251.

(14) Zhao, Y.-Q.; Liu, B.; Yu, Z.-L.; Ma, J.; Qiang Wan, Q. W.; He, P.; Cai, M.-Q. Strong Ferroelectric Polarization of $CH_3NH_3GeI_3$ with High-Absorption and Mobility Transport Anisotropy: Theoretical Study. *J. Mater. Chem. C* **2017**, *5* (22), 5356–5364.

(15) Shi, Z.; Guo, J.; Chen, Y.; Li, Q.; Pan, Y.; Zhang, H.; Xia, Y.; Huang, W. Lead-Free Organic-Inorganic Hybrid Perovskites for Photovoltaic Applications: Recent Advances and Perspectives. *Adv. Mater.* **2017**, *29* (16), 1605005.

(16) Zhao, X.-G.; Yang, J.-H.; Fu, Y.; Yang, D.; Xu, Q.; Yu, L.; Wei, S.-H.; Zhang, L. Design of Lead-Free Inorganic Halide Perovskites for Solar Cells via Cation-Transmutation. *J. Am. Chem. Soc.* **2017**, *139* (7), 2630–2638.

(17) Sun, P.-P.; Li, Q.-S.; Yang, L.-N.; Li, Z.-S. Theoretical Insights into a Potential Lead-Free Hybrid Perovskite: Substituting Pb^{2+} with Ge^{2+}. *Nanoscale* **2016**, *8* (3), 1503–1512.

(18) Ma, L.; Hao, F.; Stoumpos, C. C.; Phelan, B. T.; Wasielewski, M. R.; Kanatzidis, M. G.

Carrier Diffusion Lengths of over 500 Nm in Lead-Free Perovskite $CH_3NH_3SnI_3$ Films. *J. Am. Chem. Soc.* **2016**, *138* (44), 14750–14755.

(19) Yokoyama, T.; Song, T.-B.; Cao, D. H.; Stoumpos, C. C.; Aramaki, S.; Kanatzidis, M. G. The Origin of Lower Hole Carrier Concentration in Methylammonium Tin Halide Films Grown by a Vapor-Assisted Solution Process. *ACS Energy Lett.* **2017**, *2* (1), 22–28.

(20) Park, B.-W.; Philippe, B.; Zhang, X.; Rensmo, H.; Boschloo, G.; Johansson, E. M. J. Bismuth Based Hybrid Perovskites $A_3Bi_2I_9$ (A: Methylammonium or Cesium) for Solar Cell Application. *Adv. Mater.* **2015**, *27* (43), 6806–6813.

(21) Vargas, B.; Ramos, E.; Pérez-Gutiérrez, E.; Alonso, J. C.; Solis-Ibarra, D. A Direct Bandgap Copper–Antimony Halide Perovskite. *J. Am. Chem. Soc.* **2017**, *139* (27), 9116–9119.

(22) Kim, Y.; Yang, Z.; Jain, A.; Voznyy, O.; Kim, G.-H.; Liu, M.; Quan, L. N.; García de Arquer, F. P.; Comin, R.; Fan, J. Z.; et al. Pure Cubic-Phase Hybrid Iodobismuthates $AgBi_2I_7$ for Thin-Film Photovoltaics. *Angew. Chemie Int. Ed.* **2016**, *55* (33), 9586–9590.

(23) Hoye, R. L. Z.; Schulz, P.; Schelhas, L. T.; Holder, A. M.; Stone, K. H.; Perkins, J. D.; Vigil-Fowler, D.; Siol, S.; Scanlon, D. O.; Zakutayev, A.; et al. Perovskite-Inspired Photovoltaic Materials: Toward Best Practices in Materials Characterization and Calculations. *Chem. Mater.* **2017**, *29* (5), 1964–1988.

(24) Noel, N. K.; Stranks, S. D.; Abate, A.; Wehrenfennig, C.; Guarnera, S.; Haghighirad, A.-A.; Sadhanala, A.; Eperon, G. E.; Pathak, S. K.; Johnston, M. B.; et al. Lead-Free Organic-Inorganic Tin Halide Perovskites for Photovoltaic Applications. *Energy Environ. Sci.* **2014**, *7*, 3061–3068.

(25) Stoumpos, C. C.; Frazer, L.; Clark, D. J.; Kim, Y. S.; Rhim, S. H.; Freeman, A. J.; Ketterson, J. B.; Jang, J. I.; Kanatzidis, M. G. Hybrid Germanium Iodide Perovskite Semiconductors: Active Lone Pairs, Structural Distortions, Direct and Indirect Energy Gaps, and Strong Nonlinear Optical Properties. *J. Am. Chem. Soc.* **2015**, *137* (21), 6804–6819.

(26) Giustino, F.; Snaith, H. J. Toward Lead-Free Perovskite Solar Cells. *ACS Energy Lett.* **2016**, *1* (6), 1233–1240.

(27) Chakraborty, S.; Xie, W.; Mathews, N.; Sherburne, M.; Ahuja, R.; Asta, M.; Mhaisalkar, S. G. Rational Design: A High-Throughput Computational Screening and Experimental Validation Methodology for Lead-Free and Emergent Hybrid Perovskites. *ACS Energy Lett.* **2017**, *2* (4), 837–845.

(28) Noel, N. K.; Stranks, S. D.; Abate, A.; Wehrenfennig, C.; Guarnera, S.; Haghighirad, A.; Sadhanala, A.; Eperon, G. E.; Pathak, S. K.; Johnston, M. B.; et al. Environmental Science for Photovoltaic Applications †. *Energy Environ. Sci.* **2014**, *0*, 1–8.

(29) Hao, F.; Stoumpos, C. C.; Chang, R. P. H.; Kanatzidis, M. G. Anomalous Band Gap Behavior in Mixed Sn and Pb Perovskites Enables Broadening of Absorption Spectrum in Solar Cells. *J. Am. Chem. Soc.* **2014**, *136* (22), 8094–8099.

(30) Zhao, B.; Abdi-Jalebi, M.; Tabachnyk, M.; Glass, H.; Kamboj, V. S.; Nie, W.; Pearson, A. J.; Puttisong, Y.; Gödel, K. C.; Beere, H. E.; et al. High Open-Circuit Voltages in Tin-Rich Low-Bandgap Perovskite-Based Planar Heterojunction Photovoltaics. *Adv. Mater.* **2017**, *29* (2), 1604744.

(31) Hao, F.; Stoumpos, C. C.; Chang, R. P. H.; Kanatzidis, M. G. Anomalous Band Gap Behavior in Mixed Sn and Pb Perovskites Enables Broadening of Absorption Spectrum in Solar Cells. *J. Am. Chem. Soc.* **2014**, *136* (22), 8094–8099.

(32) Im, J.; Stoumpos, C. C.; Jin, H.; Freeman, A. J.; Kanatzidis, M. G. Antagonism between Spin–Orbit Coupling and Steric Effects Causes Anomalous Band Gap Evolution in the Perovskite Photovoltaic Materials CH 3 NH 3 Sn 1– X Pb X I 3. *J. Phys. Chem. Lett.* **2015**, *6* (17), 3503–3509.

(33) Zuo, F.; Williams, S. T.; Liang, P.-W.; Chueh, C.-C.; Liao, C.-Y.; Jen, A. K.-Y. Binary-Metal Perovskites Toward High-Performance Planar-Heterojunction Hybrid Solar Cells. *Adv. Mater.* **2014**, *26* (37), 6454–6460.

(34) Eperon, G. E.; Leijtens, T.; Bush, K. A.; Prasanna, R.; Green, T.; Wang, J. T.-W.;

McMeekin, D. P.; Volonakis, G.; Milot, R. L.; May, R.; et al. Perovskite-Perovskite Tandem Photovoltaics with Optimized Band Gaps. *Science* **2016**, *354* (6314), 861–865.

(35) Ju, M.-G.; Dai, J.; Ma, L.; Zeng, X. C. Lead-Free Mixed Tin and Germanium Perovskites for Photovoltaic Application. *J. Am. Chem. Soc.* **2017**, *139* (23), 8038–8043.

(36) Ahrens, L. H. The Use of Ionization Potentials Part 1. Ionic Radii of the Elements. *Geochim. Cosmochim. Acta* **1952**, *2* (3), 155–169.

(37) Yoder, C. H. *Ionic Compounds*; John Wiley & Sons, Inc.: Hoboken, NJ, USA, 2006.

(38) Goldschmidt, V. M. Die Gesetze Der Krystallochemie. *Naturwissenschaften* **1926**, *14* (21), 477–485.

(39) Aristidou, N.; Eames, C.; Sanchez-Molina, I.; Bu, X.; Kosco, J.; Islam, M. S.; Haque, S. A. Fast Oxygen Diffusion and Iodide Defects Mediate Oxygen-Induced Degradation of Perovskite Solar Cells. *Nat. Commun.* **2017**, *8*, 15218.

(40) Ghosh, D.; Walsh Atkins, P.; Islam, M. S.; Walker, A. B.; Eames, C. Good Vibrations: Locking of Octahedral Tilting in Mixed-Cation Iodide Perovskites for Solar Cells. *ACS Energy Lett.* **2017**, *2* (10), 2424–2429.

(41) Sadhanala, A.; Deschler, F.; Thomas, T. H.; Dutton, S. E.; Goedel, K. C.; Hanusch, F. C.; Lai, M. L.; Steiner, U.; Bein, T.; Docampo, P.; et al. Preparation of Single-Phase Films of CH3NH3Pb(I1– X Brx)3 with Sharp Optical Band Edges. *J. Phys. Chem. Lett.* **2014**, *5* (15), 2501–2505.

(42) Zhang, W.; Saliba, M.; Moore, D. T.; Pathak, S. K.; Hörantner, M. T.; Stergiopoulos, T.; Stranks, S. D.; Eperon, G. E.; Alexander-Webber, J. A.; Abate, A.; et al. Ultrasmooth Organic–inorganic Perovskite Thin-Film Formation and Crystallization for Efficient Planar Heterojunction Solar Cells. *Nat. Commun.* **2015**, *6*, 6142.

(43) Stoumpos, C. C.; Malliakas, C. D.; Kanatzidis, M. G. Semiconducting Tin and Lead Iodide Perovskites with Organic Cations: Phase Transitions, High Mobilities, and near-Infrared Photoluminescent Properties. *Inorg. Chem.* **2013**, *52* (15), 9019–9038.

(44) Hao, F.; Stoumpos, C. C.; Cao, D. H.; Chang, R. P. H.; Kanatzidis, M. G. Lead-Free Solid-State Organic-Inorganic Halide Perovskite Solar Cells. *Nat. Photonics* **2014**, *8* (6), 489–494.

(45) Lai, M. L.; Tay, T. Y. S.; Sadhanala, A.; Dutton, S. E.; Li, G.; Friend, R. H.; Tan, Z.-K. Tunable Near-Infrared Luminescence in Tin Halide Perovskite Devices. *J. Phys. Chem. Lett.* **2016**, *7* (14), 2653–2658.

(46) Jellicoe, T. C.; Richter, J. M.; Glass, H. F. J.; Tabachnyk, M.; Brady, R.; Dutton, S. E.; Rao, A.; Friend, R. H.; Credgington, D.; Greenham, N. C.; et al. Synthesis and Optical Properties of Lead-Free Cesium Tin Halide Perovskite Nanocrystals. *J. Am. Chem. Soc.* **2016**, *138* (9), 2941–2944.

(47) Liao, W.; Zhao, D.; Yu, Y.; Shrestha, N.; Ghimire, K.; Grice, C. R.; Wang, C.; Xiao, Y.; Cimaroli, A. J.; Ellingson, R. J.; et al. Fabrication of Efficient Low-Bandgap Perovskite Solar Cells by Combining Formamidinium Tin Iodide with Methylammonium Lead Iodide. *J. Am. Chem. Soc.* **2016**, *138* (38), 12360–12363.

(48) Lee, S. J.; Shin, S. S.; Kim, Y. C.; Kim, D.; Ahn, T. K.; Noh, J. H.; Seo, J.; Seok, S. Il. Fabrication of Efficient Formamidinium Tin Iodide Perovskite Solar Cells through SnF2-Pyrazine Complex. *J. Am. Chem. Soc.* **2016**, *138* (12), 3974–3977.

(49) Xing, G.; Kumar, M. H.; Chong, W. K.; Liu, X.; Cai, Y.; Ding, H.; Asta, M.; Grätzel, M.; Mhaisalkar, S.; Mathews, N.; et al. Solution-Processed Tin-Based Perovskite for Near-Infrared Lasing. *Adv. Mater.* **2016**.

(50) Galkowski, K.; Mitioglu, A.; Miyata, A.; Plochocka, P.; Portugall, O.; Eperon, G. E.; Wang, J. T.-W.; Stergiopoulos, T.; Stranks, S. D.; Snaith, H. J.; et al. Determination of the Exciton Binding Energy and Effective Masses for Methylammonium and Formamidinium Lead Tri-Halide Perovskite Semiconductors. *Energy Environ. Sci.* **2016**, *9* (3), 962–970.

TOC

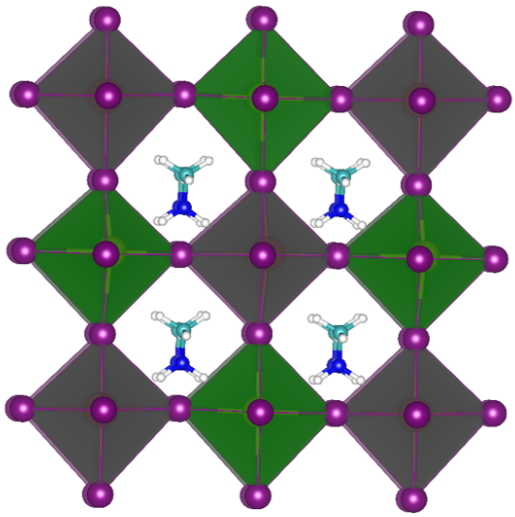

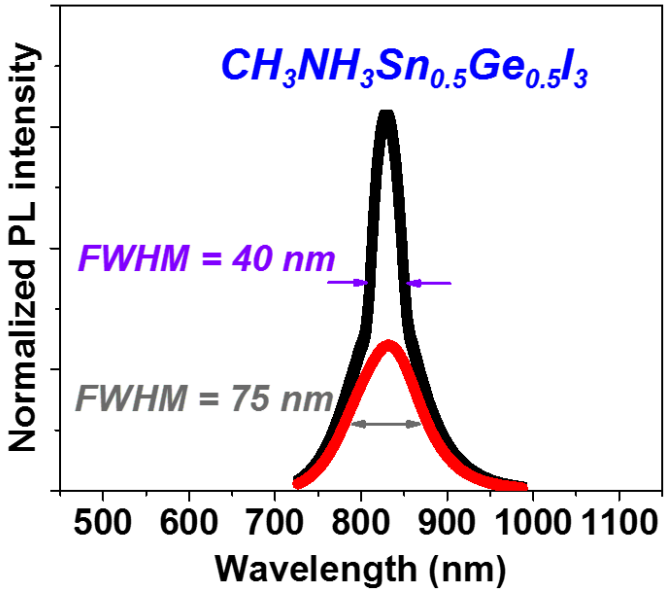
$CH_3NH_3Sn_{0.5}Ge_{0.5}I_3$
FWHM = 40 nm
FWHM = 75 nm
Normalized PL intensity
500 600 700 800 900 1000 1100
Wavelength (nm)